Spectral permittivity tensor and density functional theory calculations on the Heusler compound $Co_2FeAl_{0.5}Si_{0.5}$

Radek Ješko [1,2] Ondřej Stejskal [1,2,3,*] Robin Silber [1,2] Lukáš Beran,[3] Martin Veis,[3] Ahmad Omar,[4] and Jaroslav Hamrle [3]

[1]*Nanotechnology Centre, VŠB – Technical University of Ostrava, Ostrava, Czech Republic*
[2]*IT4Innovations, VŠB – Technical University of Ostrava, Ostrava, Czech Republic*
[3]*Faculty of Mathematics and Physics, Charles University, Prague, Czech Republic*
[4]*Leibniz Institute for Solid State and Materials Research Dresden e.V., Dresden, Germany*

The Heusler compound $Co_2FeAl_{0.5}Si_{0.5}$ is an interesting material for spintronic applications due to its predicted half-metal ferromagnetic character with a large band gap in the minority states. In this work, we present the optical and magneto-optical properties of a $Co_2FeAl_{0.5}Si_{0.5}$ bulk sample at room temperature. The spectral permittivity is found to be dominated by an absorption peak at 1.4 eV, originating mostly from absorptions by minority electrons. The best agreement between the experimentally obtained spectral permittivity tensor and the *ab initio* calculated one is for the local density approximation potential, closely followed by the generalized gradient approximation potential. However, the half-metallic ferromagnet character with 100% spin polarization is preserved only in calculations employing the Coulomb interaction correction ($+U$). This suggests that $Co_2FeAl_{0.5}Si_{0.5}$ is probably not a half metal as a single minority d-band dips below the Fermi level.

I. INTRODUCTION

Progress in the field of spintronics in recent decades has brought considerable attention to the half-metallic ferromagnets (HMFs), first described in 1983 by de Groot *et al.* [1]. Their exceptional property of 100% spin polarization at Fermi energy makes them interesting for applications in spintronic devices where efficient spin injection and detection at room temperature is necessary. HMFs such as Fe_3O_4, CrO_2, $La_{1-x}Sr_xMnO_3$, etc. have been intensively studied, leading to the tunneling magnetoresistance (TMR) ratio of a few percent at room temperature [2–4].

Another HMF class of materials is Co_2-based Heusler compounds, which are predicted to be half metallic with a wide band gap in the minority states [5–9]. These materials show high Curie temperatures up to 1100 K, as reported for Co_2FeSi [10], and tunability of their structural, electric, and magnetic properties [7] with stoichiometry. Fermi-level tuning of $Co_2FeAl_xSi_{1-x}$ [11] indicated particular temperature robustness of $Co_2FeAl_{0.5}Si_{0.5}$ (CFAS) due to the Fermi level located in the middle of the electronic band gap [12]. This has led to high TMR of 386% at 300 K (and 832% at 9 K) for a magnetic tunnel junction with CFAS electrodes [13], which markedly exceeded the observed TMR for conventional 3d transition-metal ferromagnetic electrodes [14]. This has made CFAS a material of particular interest and has led to intensive research in the fields of structural and magnetic properties [15–17], magneto-optics [18], spin dynamics [19], spin-orbit torques [20], and spin pumping [21]. There have been several attempts to investigate the band gap of CFAS and Heuslers

with similar composition experimentally [22–24], but the results differ from theoretically predicted values [12,25].

Here we investigate the spectral dependence of the permittivity tensor of CFAS, i.e., its optical and magneto-optical behavior in an extended visible photon range. The presented results of spectrally dependent optical and magneto-optical properties are obtained by spectroscopic ellipsometry and magneto-optical Kerr effect (MOKE) spectroscopy. The obtained permittivity spectra were compared to *ab initio* calculations with several implemented exchange-correlation potentials, with or without the Hubbard U Coulomb interaction correction [26].

The text organization is as follows. Section II introduces the sample preparation and its structural and magnetic properties. Section III presents the results of optical and linear magneto-optical measurements of the sample permittivity tensor, including the optical oscillator model. Section IV follows with *ab initio* calculations of the spectral permittivity tensor for various exchange-correlation potentials. In Sec. V, all models are compared to each other and to the experiments. In Sec. VI, the dependence of the results on the U value is discussed. In Sec. VII, the results are discussed in relation to other investigations. The Supplemental Material [27] contains a detailed description of the oscillator functions equations for diagonal permittivity and their fitted values. It also contains additional *ab initio* band structures of the local density approximation (LDA) and LDA+U and structural details by x-ray diffraction (XRD) Rietveld refinement.

II. SAMPLE PREPARATION AND NONOPTICAL CHARACTERIZATION

The polycrystalline bulk samples of CFAS were prepared by arc melting of stoichiometric quantities of at least 4N
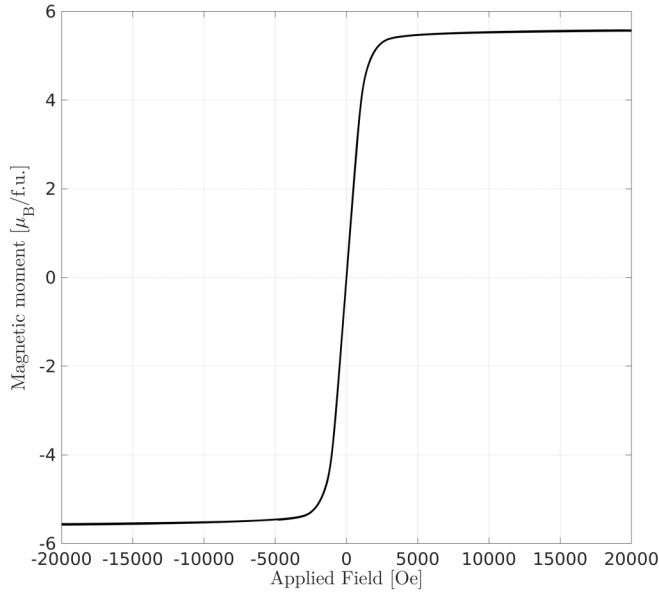
*stejskal@karlov.mff.cuni.cz

FIG. 1. The SQUID magnetization hysteresis curve of CFAS at room temperature.

pure constituents in argon atmosphere. Before melting, the working chamber was evacuated to 10^{-5} mbar pressure and refilled with argon. This process was repeated multiple times to minimize oxygen contamination. Additionally, a titanium getter was melted three times to ensure minimal oxygen content in the chamber before the actual sample melting process. The sample pellets were flipped and remelted three times to achieve better homogenization. Subsequent annealing was carried out in sealed evacuated quartz tubes, which were evacuated to 10^{-5} mbar and refilled with argon three times before the sealing to ensure minimal oxidation during the annealing process. The samples were annealed for seven days at 1000 °C and then furnace cooled to room temperature.

Both the as-cast and annealed polycrystalline samples were cut, polished, and analyzed using the Nova-NanoSEM (FEI/Thermo Fisher Scientific) high-resolution scanning electron microscope with an energy-dispersive x-ray (EDX) analyzer. Structural characterization was done by the XRD on powder samples using the STOE STADI diffractometer in transmission geometry with Mo $K_{\alpha 1}$ radiation, a germanium monochromator, and a DECTRIS MYTHEN 1 K detector. For the XRD investigation of powdered samples, the arc-melted pellets were crushed using a stainless-steel mortar by hand. For the Rietveld refinement of the XRD data, the FULLPROF software package was used [28]. The magnetic properties were investigated by a superconducting quantum interference device (SQUID, Quantum Design MPMS-XL-5).

EDX analysis showed that the stoichiometry of the sample is sufficiently close to the nominal one (Co 48.4 ± 0.6 at.%; Fe 24.5 ± 0.2 at.%; Al 13.0 ± 0.3 at.%; Si 14.1 ± 0.3 at.%). SQUID magnetometry at 5 K shows that the total saturation magnetic moment is 5.62 μ_B/f.u., which fits well to the previously calculated saturation moment results [12,29]. The saturation magnetic moment at room temperature was determined to be 5.57 μ_B/f.u. The SQUID magnetization hysteresis curve is shown in Fig. 1.

XRD shows that although the as-cast sample is highly *B*2 ordered (see the Supplemental Material [27]), the annealed sample shows a high and narrow (111) peak, suggesting predominantly *L*2$_1$-type ordering. Rietveld refinement was performed to evaluate the exact structural parameters and the ordering fraction using the $Fm\bar{3}m$ space group (see details in the Supplemental Material [27]). The lattice constant was fitted to 0.5687(2) nm with a residual *B*2 order fraction of 28%. This fits well with the predicted most thermodynamically stable ordering profile [30]. The calculations show that even up to 50% *B*2 disorder, the half metallicity is preserved and the saturation magnetization is unaffected [30].

III. SPECTRA OF THE PERMITTIVITY TENSOR ELEMENTS

The optical and magneto-optical response of a material is described by the permittivity tensor ε_{ij}. The sample magnetization is accompanied by the time-reversal symmetry breaking, leading to anisotropy in ε_{ij}. To describe the permittivity tensor, we use the linear magneto-optical approximation. Thus, only the constant and the linear terms of the Taylor series expansion in magnetization **M** are considered:

$$\varepsilon_{ij} = \varepsilon_{ij}^{(0)} + K_{ijk}M_k = \varepsilon_{ij}^{(0)} + \varepsilon_{ij}^{(1)}, \quad (1)$$

where $\varepsilon_{ij}^{(0)}$ is the permittivity tensor independent of magnetization direction, K_{ijk} is the magneto-optical permittivity tensor linear in magnetization, and M_k are components of normalized **M**. In the case of a cubic material, $\varepsilon_{ij}^{(0)}$, K_{ijk} simplifies to [31,32]

$$\varepsilon_{ij}^{(0)} = \varepsilon^{(0)}\delta_{ij}, \quad K_{ijk} = K\epsilon_{ijk}, \quad (2)$$

where $\varepsilon^{(0)}$, K, δ_{ij}, and ϵ_{ijk} are the diagonal permittivity, the magneto-optical permittivity (describing magneto-optic spectra linear in **M**), the Kronecker delta, and the Levi-Civita tensor, respectively.

A. Diagonal permittivity probed by ellipsometry

Spectroscopic ellipsometry was performed on one of the annealed polycrystalline bulk samples shortly after repolishing to avoid an excessive oxidation layer on its surface. The measurements were performed in the spectral range from 0.73 to 6.42 eV for a set of different angles of incidence from 45° to 75°, with a 5° step on a Woollam RC2-DI Mueller matrix ellipsometer. The spectra of ellipsometric parameters Ψ and Δ for the angle of incidence 60° are shown in insets (d) and (e) of Fig. 2, respectively. In the following, we express the experimental ellipsometry spectra by the pseudodielectric function $\varepsilon_{pseudo}^{(0)}$, being isomorphically related to Ψ and Δ [33]. The real and imaginary parts of $\varepsilon_{pseudo}^{(0)}$ for the angle of incidence 60° are shown in Figs. 2(a) and 2(b), respectively.

To obtain the diagonal permittivity $\varepsilon^{(0)}$ of bulk CFAS, the appropriate optical model of the sample has to be used. This model separates the individual sample feature contributions (surface roughness, possible oxidation layers on the substrate, etc.) from the overall ellipsometric response (Ψ and Δ or, equivalently, $\varepsilon_{pseudo}^{(0)}$) and allows the extraction of optical properties of the investigated material. In our case, we model surface roughness on top of bulk CFAS by the effective
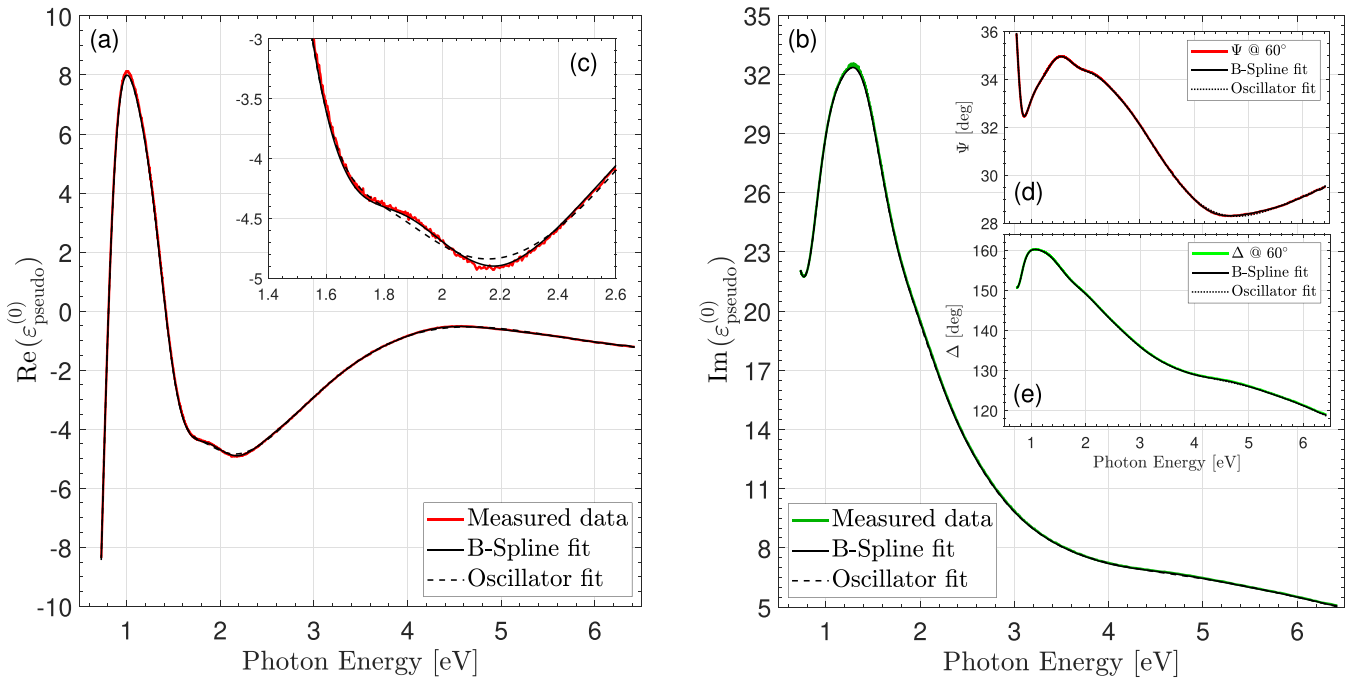
FIG. 2. Ellipsometric spectra of CFAS in the form of the pseudodielectric function $\varepsilon_{\mathrm{pseudo}}^{(0)}$. Solid (a) red and (b) green lines represent experimental $\mathrm{Re}(\varepsilon_{\mathrm{pseudo}}^{(0)})$ and $\mathrm{Im}(\varepsilon_{\mathrm{pseudo}}^{(0)})$, respectively. Solid and dashed black lines represent B-spline and oscillator model fits, respectively. In inset (c), the magnified part of the spectra around 2 eV is shown, where the deviation of the oscillator model was largest. Insets (d) and (e) show the corresponding ellipsometry spectra expressed by ellipsometric parameters Ψ and Δ with the respective fits. Only spectra for the angle of incidence 60° are presented.

medium approximation (EMA). The surface roughness was measured by atomic force microscopy (AFM) as $R_a = 3.74$ nm (roughness average) with the root mean square $R_{\mathrm{RMS}} = 4.80$ nm, measured as a mean value on areas of $25 \times 25\ \mu\mathrm{m}^2$.

Two different models are employed to acquire the diagonal permittivity $\varepsilon^{(0)}$ of CFAS, i.e., the B-spline model and the oscillator model. First, the B-spline [34] (basis spline) is a purely mathematical determination of the diagonal permittivity spectral function found by fitting the experimental spectra (Ψ and Δ, or $\varepsilon_{\mathrm{pseudo}}^{(0)}$) and satisfying the Kramers-Kronig relations. This model gives the most precise fit, but provides limited physical background. The AFM values of surface roughness were used as an input to the fit. The permittivity $\varepsilon^{(0)}$ obtained by the B-spline fit is shown in Fig. 3 by a solid orange line. Agreement of the fit with the experimental spectra represented by $\varepsilon_{\mathrm{pseudo}}^{(0)}$ is shown in Fig. 2 as solid black lines.

Second, the oscillator model consists of the sum of contributing spectral functions reflecting features in the electronic structure of the material. The oscillator model used here includes five contributions: Drude term, Tauc-Lorentz oscillator, Gauss oscillator, and two Lorentz oscillators. The mathematical form of the individual oscillators [35–41] with the obtained model parameters are given in the Supplemental Material [27]. We used the surface roughness as a fitted (free) parameter and obtained 5.2 nm, which is close to the AFM roughness value. The permittivity $\varepsilon^{(0)}$ obtained by the oscillator model is shown in Fig. 3 by a dash-dotted black line. The agreement of the fit with the experimental spectra $\varepsilon_{\mathrm{pseudo}}^{(0)}$ is shown in Fig. 2 by dashed black lines. The oscillator model allows extrapolation of the permittivity to the infrared and ultraviolet spectral range, as it is based on the analytic

relation between permittivity and photon energy. The validity of this extrapolation to the infrared range is confirmed by the Fourier-transform infrared spectroscopy (FTIR) reflection measurement (Fig. 4).

The contributions of individual oscillators are shown in Fig. 3. The Drude term describes the contribution of free carriers to the permittivity and it dominates in the infrared region. In the case of HMF, these free charges correspond to the majority spin electrons on the Fermi surface. The Lorentz oscillator model was developed to describe light absorption between two distinct electronic levels. However, in a solid state, the Lorentz oscillators are used to account for numerous electric dipole transitions (for both majority and minority electrons) present in the electronic structure. The Tauc-Lorentz function was developed to fit optical parameters of amorphous semiconductors and insulators and is therefore suitable for fitting band-gap-related phenomena. As the minority electrons' band gap is expected, we use the Tauc-Lorentz oscillator to describe the optical properties near this band gap. From the fit, a band gap of 742 meV was obtained. An additional oscillator was required to fit the experimental spectra, and hence the Gaussian oscillator was used. The small Gaussian peak further enhances the asymmetric shape of Tauc-Lorentz to describe minority electron transitions in the vicinity of the band gap. In Fig. 3, the sum of Tauc-Lorentz and Gaussian is also shown as together they model the optical response of the band gap. The key values are summarized in Table I.

The oscillator model lies in between the rigorous mathematical nature of the B-spline and the physically precise calculations from first principles, which, however, lack a
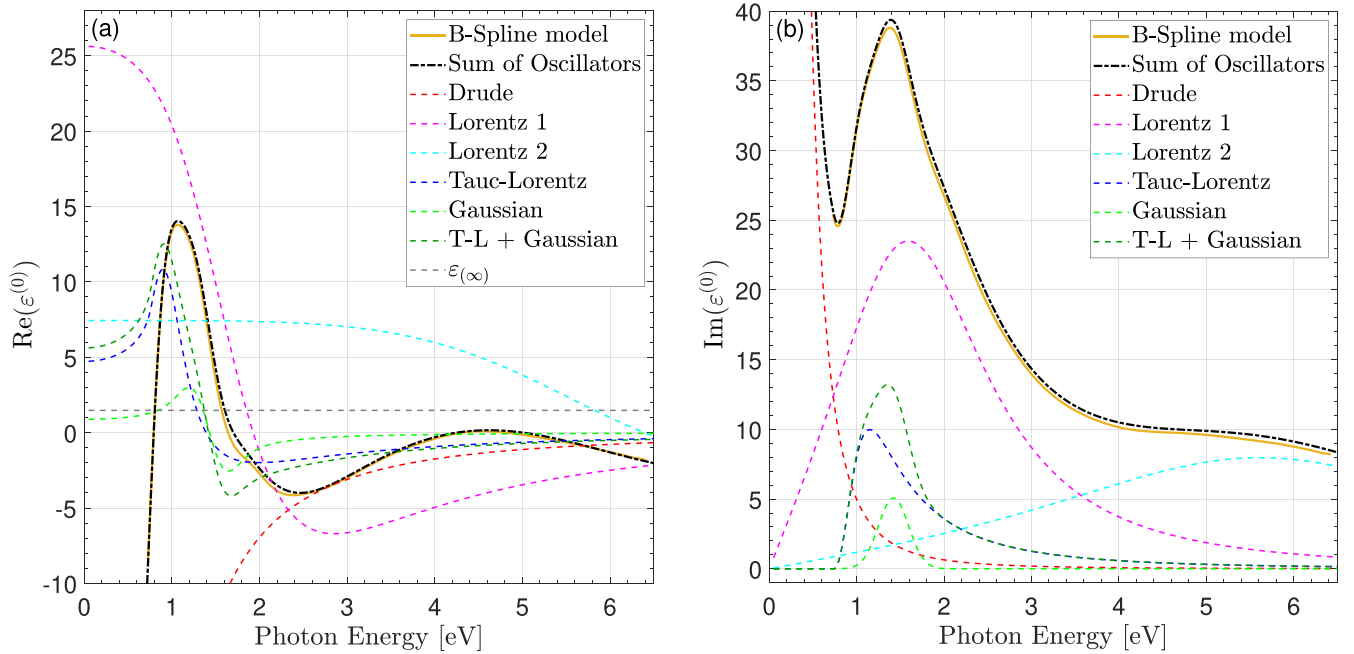
FIG. 3. (a) Real [Re($\varepsilon^{(0)}$)] and (b) imaginary [Im($\varepsilon^{(0)}$)] part of the diagonal permittivity of CFAS. The solid orange line corresponds to the B-spline model and the black dash-dotted line corresponds to the oscillator model. Dashed lines correspond to the individual contributions of the oscillator model. The sum of the Gaussian and Tauc-Lorentz (T-L) oscillator describing the contribution of the minority spin electrons' interband transitions around the energy gap is also shown.

simple inside view. It turns out that five oscillators were the least amount needed to obtain almost perfect agreement with the ellipsometric measurement, with the highest relative deviation around 2 eV, as shown in Fig. 2(c).

The oxide cap layer was omitted in the used optical model, as its presence was found to have a negligible effect on the key values. For example, if a 2 nm oxidation layer is assumed on top of CFAS with optical constants of CoO [42], then the position of the main peak increases by 0.046 eV, i.e., by 3%. Also note that we have remeasured the ellipsometry spectra four years after the polishing with the sample not stored in vacuum. Those spectra suggest an increase of the thickness of the oxide cap layer by 2 nm during this period. Thus, we assume the thickness of the oxide cap layer to be below 2 nm when the ellipsometry spectra were measured right after the polishing.

B. Magneto-optical permittivity probed by MOKE spectroscopy

We performed MOKE spectroscopy in the polar configuration (i.e., with out-of-plane sample magnetization) using a general MOKE ellipsometer with rotating analyzer and external magnetic field of 1.2 T. The spectra were acquired at room temperature and with a near-to-normal angle of incidence (3°). Spectra of Kerr angles are shown in Fig. 5. The Kerr rotation θ_K reaches a maximum of 0.5° at 1.6 eV, while the Kerr ellipticity ε_K has a minimum of $-0.4°$ at 1.4 eV. The spectra are compared to the obtained calculations via

$$\theta_K + i\varepsilon_K = \frac{K}{\sqrt{\varepsilon^{(0)}}(1 - \varepsilon^{(0)})}, \qquad (3)$$

for various exchange-correlation potentials (introduced below). The Drude term was added and its exact form can be found in the Supplemental Material [27].

From the measurements, spectra of the magneto-optical permittivity $K = \varepsilon_{12} = -\varepsilon_{21}$ [Figs. 6(a) and 6(b)] were determined by fitting to the standard Yeh's 4×4 matrix formalism, with diagonal permittivity taken from the B-spline model.

TABLE I. Experimental and calculated values of magnetic moments, band-gap energies, and main peak positions.

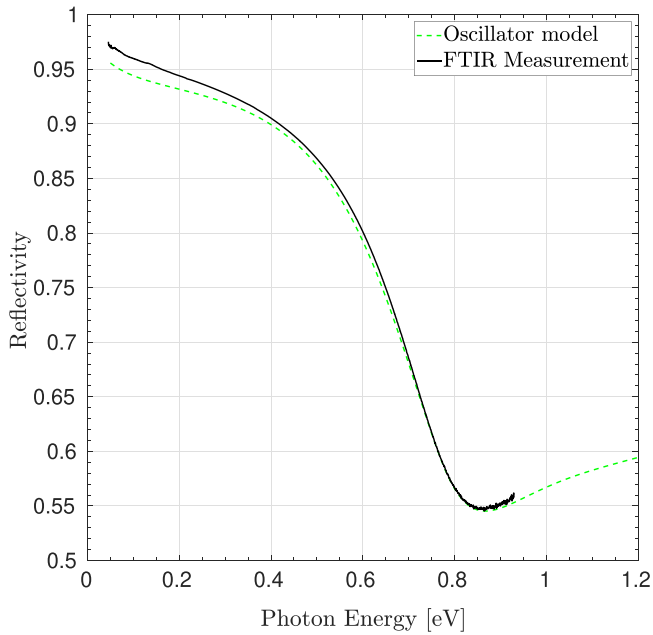| Method	Total magnetic moment (spin+orbital) (μ_B/f.u.)	Electronic band gap (eV)	Optical band gap (eV)	Absorption surge (eV)	Im($\varepsilon^{(0)}$) main peak position (eV)
Experiment	5.620			0.742	1.40
LDA	5.294 = 5.195+0.099		0.11	0.73	1.66
LDA+U	5.619 = 5.496+0.123	0.415	0.585	1.15	1.90
GGA	5.457 = 5.367+0.090		0.20	0.83	1.74
GGA+U	5.607 = 5.497+0.110	0.758	0.939	1.32	1.93

FIG. 4. Black line: Measured reflectivity of $Co_2FeAl_{0.5}Si_{0.5}$ by FTIR (Fourier-transform infrared spectroscopy). Green line: Reflectivity calculated from the oscillator model extrapolated to the IR region.
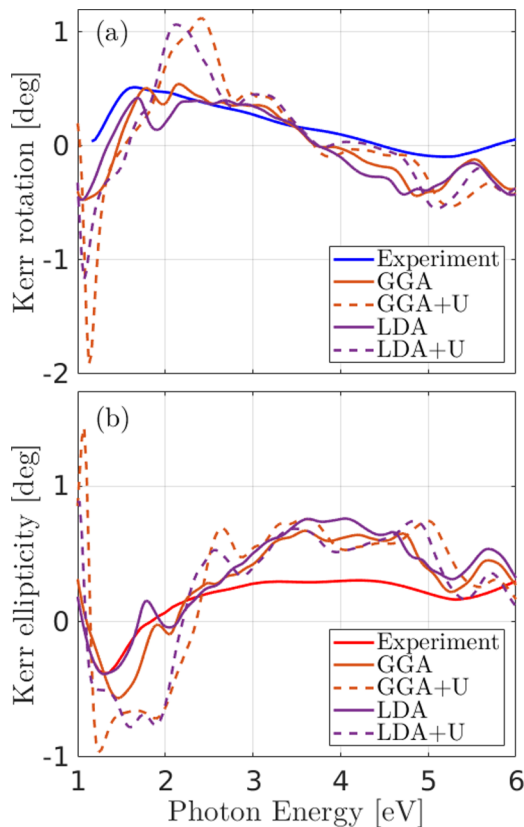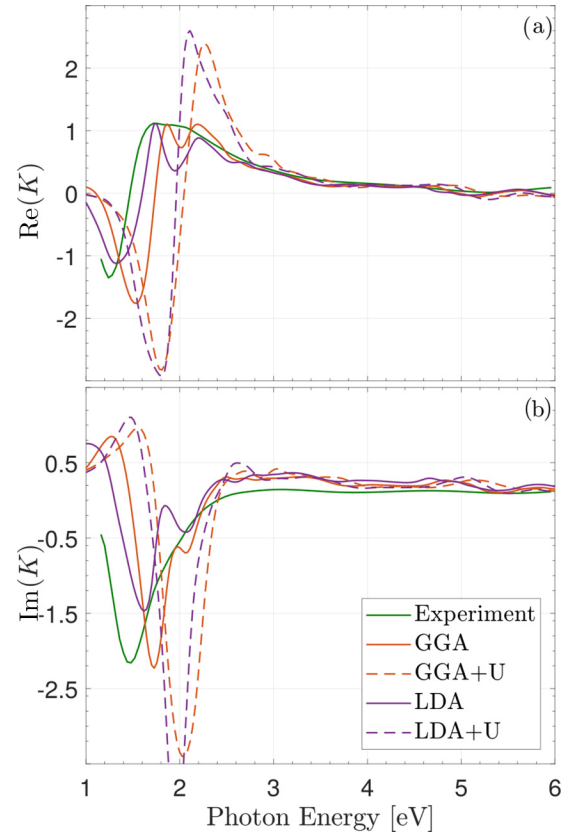
FIG. 6. (a) Real and (b) imaginary parts of the magneto-optical permittivity K determined from the fit to the experimental MOKE spectra (green) and from *ab initio* calculations (orange and purple).

IV. *AB INITIO* CALCULATIONS

The electronic structure of CFAS is calculated by the linearized augmented plane-wave method using the WIEN2K code [43]. We employed two exchange-correlation potentials, namely, local density approximation (LDA) and generalized gradient approximation (GGA) with Perdew-Burke-Ernzerhof (PBE) parametrization, and also Hubbard U correction variants for strongly correlated systems, which resulted in four distinct models denoted henceforth as GGA, GGA+U, LDA, and LDA+U. The values for the Hubbard U correction were taken from [12,44] as $U_{eff} = 1.9$ (1.8) eV for Co (Fe). The spin-orbit coupling was included using the second variation approach [43]. In the calculations, we assumed $L2_1$ ordering of the crystal structure, represented by the space group $Fm\bar{3}m$ and the mixture of Al and Si on the $4b$ sublattice was treated by the virtual crystal approximation with virtual element atomic number of 13.5. The lattice parameter 5.678 Å was taken from the Rietveld refinement of the XRD data. The electronic structure was calculated with a mesh of 27 000 k points in the full Brillouin zone. Calculations were performed at 0 K with no elevated temperature approximation considered. The important numerical results for different exchange-correlation potentials are summarized in Table I.

The diagonal and magneto-optical permittivity spectra are calculated within the electric dipole approximation using the Kubo formula [45,46] on a finer mesh of 64 000 k points in the full Brillouin zone to increase the integration precision.
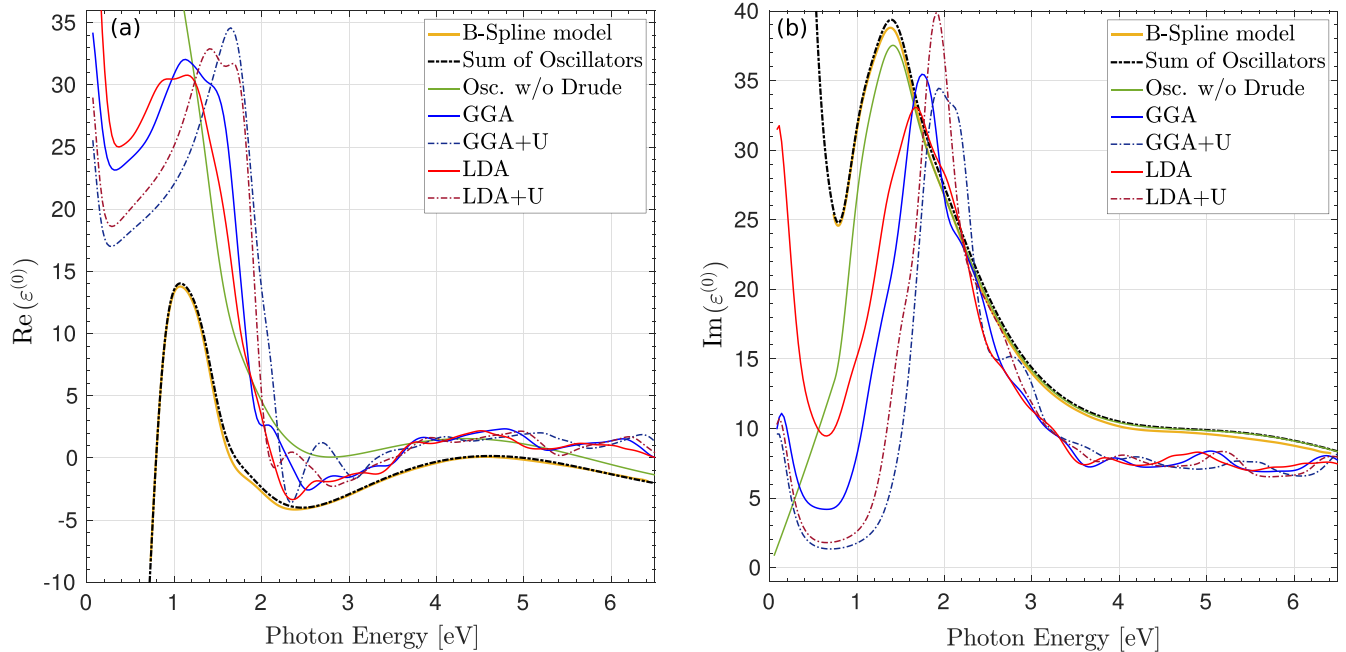
FIG. 5. (a) Spectral Kerr rotation and (b) Kerr ellipticity obtained by polar MOKE measurement at 1.2 T and 3 ° incident angle. The spectra are compared to *ab initio* calculated Kerr angles.

FIG. 7. *Ab initio* calculated (a) real and (b) imaginary diagonal permittivity $\varepsilon^{(0)}$ for different exchange-correlation potentials compared to the experimentally obtained permittivity (orange line and dashed black line) and permittivity with omitted Drude term (green line).

Using the Lorentz broadening value $\gamma = 0.1$ eV for optical and magneto-optical spectra (to account for finite lifetimes of the excited states) and applying the Kramers-Kronig relations, the full permittivity tensor is obtained. This approach provides solely direct interband contributions to the permittivity tensor. The conduction electrons' contributions (also called Drude term or intraband transitions) and indirect optical transitions are not included. The standard approach of incorporating the intraband contributions relies on the determination of a single plasma frequency and the addition of the phenomenological Drude contribution to the interband spectra [47]. However, this approach is not *ab initio* and is burdened by additional assumptions. Correct incorporation of the Drude term involves more elaborate models [47–49]. In our calculations, the inclusion of the Drude term would contribute to better agreement with the experiment, especially for low energies, but would not be of any significance towards the discussion of the performance of individual models and the half metallicity of CFAS. Therefore, we omit the Drude term in the following discussion.

Figure 7 shows the comparison between the measured and calculated diagonal permittivity $\varepsilon^{(0)}$ spectra. The position of the main absorption peak around 1.4 eV in the Im($\varepsilon^{(0)}$) part is not well reproduced by any of the used potentials. This can be attributed to the employed exchange-correlation potentials as the major approximations present in the density functional theory (DFT) that do not accurately describe the actual exchange-correlation energy of the true many-electron system [50,51]. The closest peak positions are provided by the LDA potential at 1.66 eV, closely followed by GGA at 1.74 eV (see Table I, last column). The Hubbard U correction for both potentials shifts the peak position towards higher energies by approximately an additional 0.2 eV. Apart from the shift, there is a solid agreement between the experimental and theoretical spectra.

In Fig. 6, the comparison between the measured and calculated magneto-optical permittivity K is shown. For a cubic crystal with magnetization assumed in the z direction, the K directly correspond to the off-diagonal element of the permittivity tensor ε_{xy}. Note that Re(K) is the fundamental (absorption) part of K, whereas Im(K) is the dispersion part determined by the Kramers-Kronig relations. The position of the first peak at around 1.3 eV in Re(K) is well described by LDA (GGA), being shifted only by 0.1 eV (0.3 eV). Both LDA and GGA also well describe the existence of the additional two peaks at 1.7 and 2.1 eV (even though these are much better pronounced in the calculation), as well as the overall strength of the Re(K). LDA+U and GGA+U provide the main peak shift of about 0.5 eV for both, similar to the case of $\varepsilon^{(0)}$. Also, the overall shape of the spectra and strength of the peaks are not well reproduced by the LDA+U or GGA+U potentials. It is therefore apparent that for the description of the magneto-optical spectra, both potentials without the U correction give better results, similar to the case of the optical spectra, with the best agreement provided by LDA.

A. Saturation magnetization

It is widely known that Hubbard U corrections tend to fail for systems with more delocalized electrons, such as metals [52]. However, their main success for HMF is the correct prediction of the magnetic moment. The experimental value of the total magnetic moment was measured to 5.62 μ_B/f.u. As calculated by Gercsi and Fecher [12,25], the Slater-Pauling rule [53,54] (without spin-orbit coupling) predicts saturation magnetization of 5.5 μ_B/f.u., a value close to the experimental one.

The calculated total magnetic moments per formula unit for all *ab initio* models are shown in the second column of
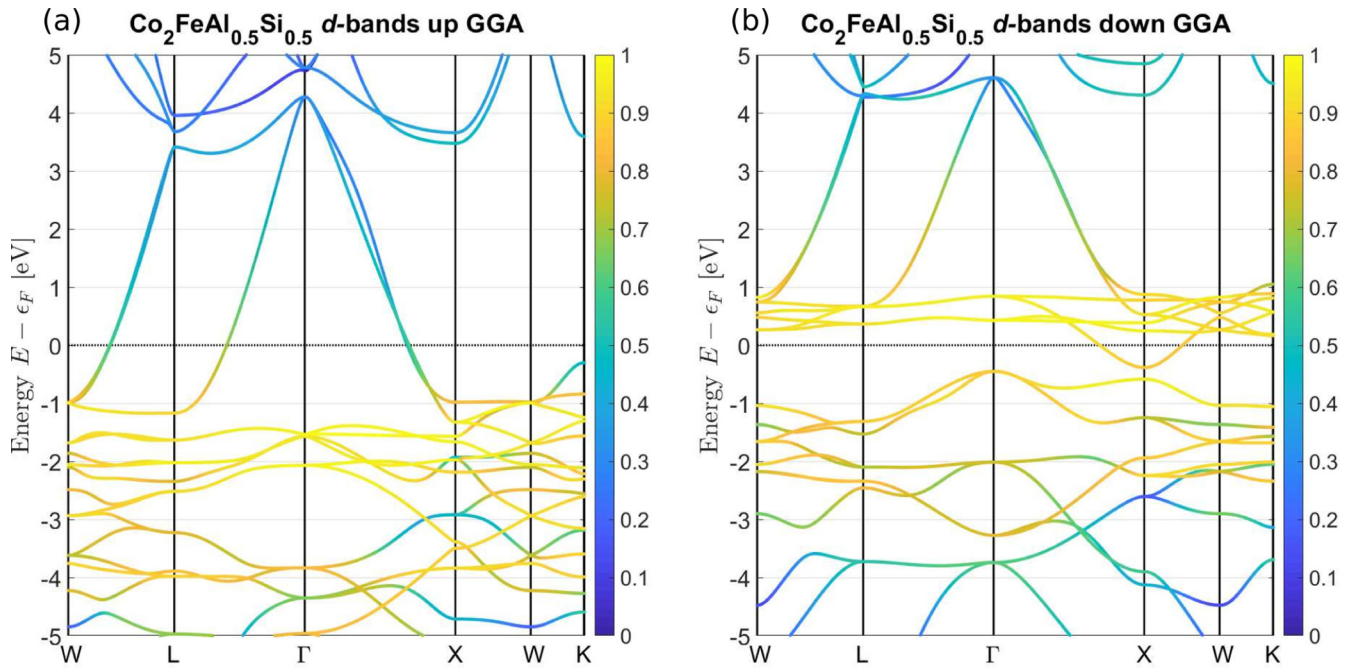
FIG. 8. Calculated band structure of $Co_2FeAl_{0.5}Si_{0.5}$ for (a) majority and (b) minority spin electrons by GGA. The color code denotes projection to electron d-states.

Table I, along with their spin and orbital parts. The spin-orbit coupling increases the total magnetic moment by an orbital part of about 0.1 μ_B/f.u. [55]. LDA and GGA provide values of 5.294 and 5.457 μ_B/f.u., which are smaller by 5.8% and 2.9%, respectively, when compared to the experimental value of 5.620 μ_B/f.u. GGA+U and LDA+U both provide the spin part of the magnetic moment of about 5.5 μ_B/f.u., as predicted by the Slater-Pauling rule. The orbital part adds an additional 0.110 and 0.123 μ_B/f.u., which in total provides saturation magnetization of 5.607 and 5.619 μ_B/f.u., respectively, which agrees perfectly with the experimental value measured at 5 K.

Thus, both $+U$ potentials perform excellently in the prediction of the magnetic moment, but fail significantly in the optical and magneto-optical spectra. In the following discussion, we compare GGA and GGA+U potentials, while the results for LDA and LDA+U are shown in the Supplemental Material [27]. The GGA potential performs best overall, providing solid spectral agreement simultaneously with an acceptable magnetic moment. Finally, only the Hubbard U corrected potentials exhibit half-metallic character, as shown by Fecher *et al.* [12].

B. Band structure and density of states

The spin-resolved band structure for the GGA potential is presented in Fig. 8. No band gap, and hence no half metal, is predicted. The colors correspond to the d-character of the bands, i.e. projection to orbital angular momentum $l = 2$. In Fig. 9, the spin-resolved band structure for GGA+U is shown, providing an indirect band gap of 0.758 eV and hence half-metallic behavior. We also present the angular momentum selective density of states (DOS) in Figs. 10(a) and 10(b). The discussion of these in the context of the optical and magneto-optical spectra, experimental results, and optical models is the subject of the next section.

V. BAND-GAP ANALYSIS

We start the discussion with definitions of electronic and optical band gaps that play a major role in the interpretation of the results. The absorption surge defined here is crucial in the following analysis of our optical experiments.

(i) Electronic band gap: or, simply, band gap is an energy range in a solid where no electronic states can exist, i.e., the energy difference between the top of the valence band and the bottom of the conduction band. If the momentum of the lowest-energy state in the conduction band and the highest-energy state of the valence band are the same, the material has a direct band gap [Fig. 11(a)] and the band gap equals the optical band gap. If they are not the same, then the material has an indirect band gap [Fig. 11(b)] and its value is smaller than the optical band gap.

(ii) Optical band gap: the energy of the lowest direct interband transition from the state below the Fermi level to the state above the Fermi level. It corresponds to the energy where the interband permittivity becomes nonzero. The optical band gap also exists in materials with no electronic band gap, as demonstrated in Figs. 11(c) and 11(d). In this case, however, there are possible intraband (Drude) transitions that contribute to the optical response (permittivity), and the presence of such optical gap exhibits as an increase in the optical absorption.

(iii) Absorption surge: the energy where the intensity of interband optical transitions suddenly increases and becomes detectable by the applied optical method. In the case of a half metal, the optical absorption due to the conduction majority electrons (Drude) is disrupted by minority electron transitions to such extent that it can be clearly differentiated from the Drude term as a separate optical contribution using techniques such as ellipsometry or reflectometry.

The optical response originating in the vicinity of the Fermi level for minority electrons is described by the
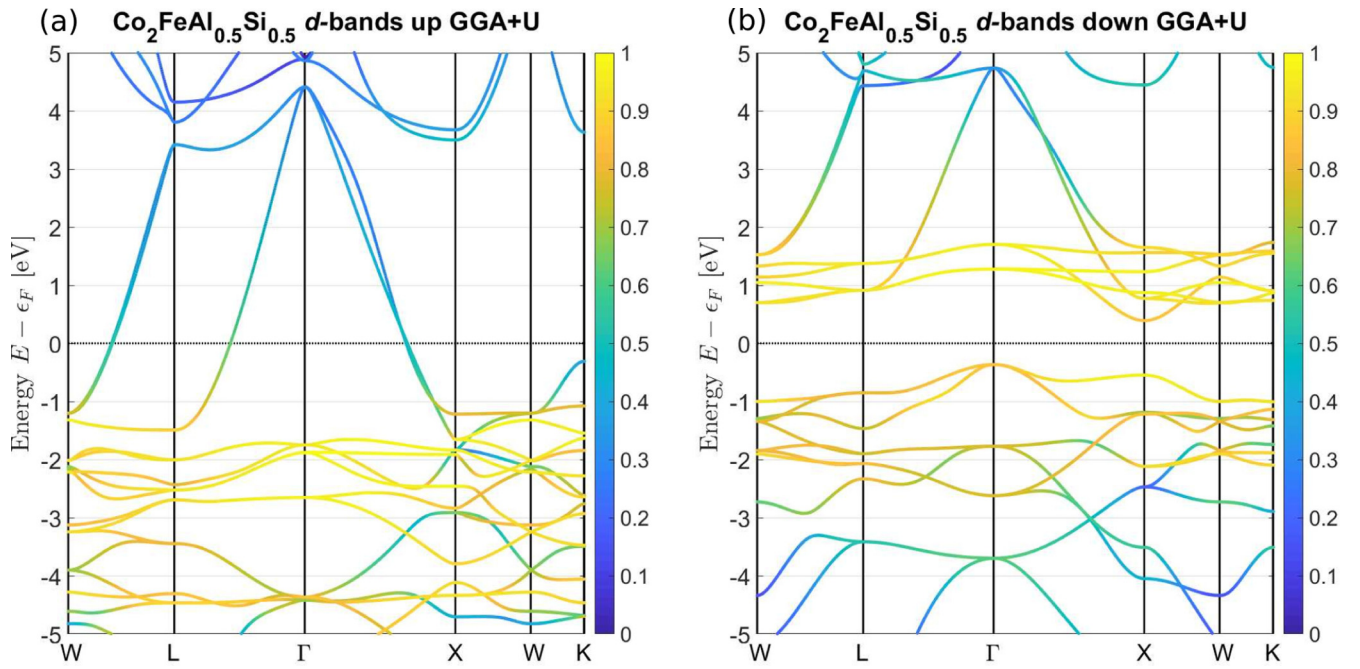
FIG. 9. Calculated band structure of $Co_2FeAl_{0.5}Si_{0.5}$ for (a) majority and (b) minority spin electrons by GGA+U. The color code denotes projection to electron d-states.

Tauc-Lorentz and Gaussian oscillators in the oscillator model (Fig. 3). These oscillators are superimposed on the Drude term and the Lorentz oscillator, both describing majority electron transitions. It is, therefore, difficult to separate by spin-indistinguishable methods, such as ellipsometry. The oscillator model gives the value of 0.74 eV as the initial point of the Tauc-Lorentz oscillator, but this value shall not be associated with the electronic band gap. Furthermore, the steep increase in absorption indicates that this value actually corresponds to the absorption surge.
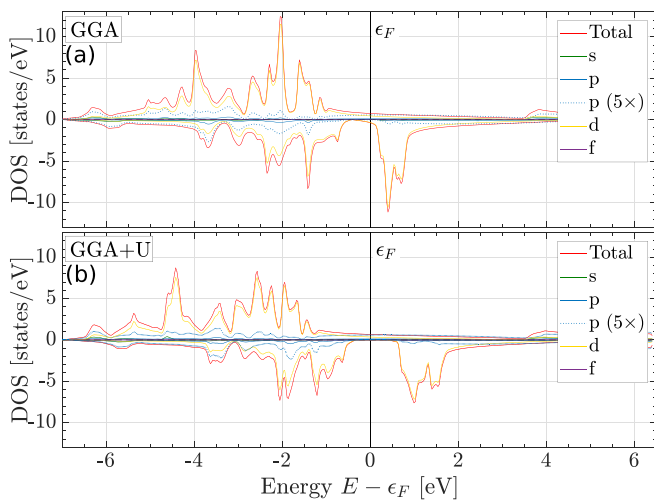

FIG. 10. Angular momentum-selective DOS obtained by (a) GGA and (b) GGA+U calculations, respectively. The p-states are also shown, multiplied by a factor of 5 for clarity. The majority spin DOS is represented by positive numbers and the minority spin DOS is represented by negative numbers.

Ab initio calculations allow for separation of majority and minority absorptions. Hence, we show the minority transitions as $\varepsilon^{(0)}_{\text{minority}}$ for both GGA and GGA+U in Fig. 12. The permittivity is presented without broadening and also as a square root for a clearer distinction of the optical band gap and absorption surge. In the case of the GGA potential, no electronic band gap is present at the Fermi level, and the value of the optical gap is 0.20 eV, which corresponds to the absorption of type (d) from Fig. 11 situated between points X and W in the band structure in Fig. 8(b). The value of the absorption surge is determined to be 0.83 eV, where the absorptions increase abruptly. This is very close to 0.74 eV obtained by the oscillator model. The main absorption peak in the optical spectra at 1.74 eV comes from the energetic difference of the occupied and excited minority d-states in the band structure, which is better demonstrated in the DOS [Fig. 10(a)]. It still overestimates the experimental ellipsometric value of 1.40 eV. Note that the selection rules forbid dipole transitions among d-states; however, electrons below -1 eV lose their almost pure d-character as shown in the band structure [Fig. 8(b); the yellow color turns greenish].

The addition of the Hubbard U increases the energetic difference of the occupied and excited d-states even more, creating an indirect band gap of 0.758 eV [Fig. 9(b)]. The optical band gap was determined to be 0.939 eV at point X and the absorption surge to 1.32 eV [see Fig. 12(b)]. The main absorption peak is at 1.93 eV, corresponding to the separation in the DOS [Fig. 10(b)]. All values, including the ones for LDA and LDA+U potentials (see Supplemental Material [27]), are compared in Table I.

These results show that GGA is superior to GGA+U in the description of the optical and magneto-optical spectra. Even GGA overestimates the separation of the occupied and excited d-states, which experimentally corresponds to the
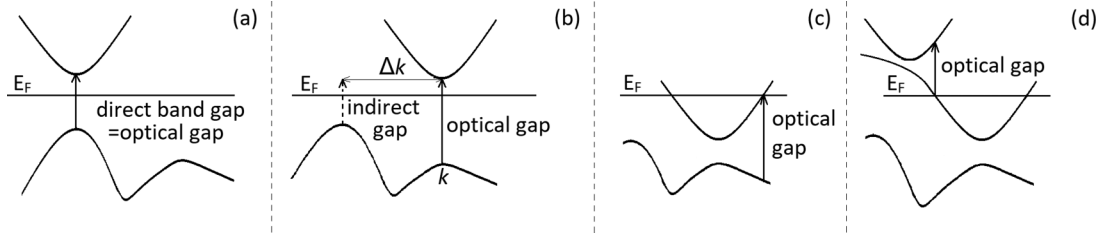
FIG. 11. Schematics of different gaps with solid vertical arrows indicating optical band gaps. (a) The direct gap in the electronic band structure equals the optical band gap. (b) Indirect band gap in the band structure. The optical gap is larger in energy, and in this schematic appears at point k. (c) No electronic band gap at the Fermi level and the optical band gap is from the valence band to the conduction band at the Fermi level. (d) No electronic band gap at the Fermi level and the optical band gap is from the conduction band at the Fermi level to the higher conduction band.

main absorption peak at 1.40 eV. This indicates that these states should be clumped together even more closely, by about 0.34 eV, suggesting minority electronic states at the Fermi level. Therefore, CFAS is most likely not a HMF, with a pocket of minority electrons around point X.

VI. DEPENDENCE ON HUBBARD U

So far, we have been using only the single value of Hubbard $U_{\mathrm{eff}} = 1.9$ (1.8) eV for Co (Fe) from [12,44]. In order to analyze the dependence of the investigated parameters on U, calculations for several U values were performed. U_{eff} for Co is varied linearly from 0 to 2.66 eV, and U_{eff} for Fe from 0 to 2.52 eV, keeping their ratio constant. The results are shown in Fig. 13 and also in the Supplemental Material [27] in Table I in tabular form.

The value of the spin magnetic moment saturates as the electronic band gap opens up at $U_{\mathrm{eff}} = 1.14$ eV, while the orbital part of the magnetic moment increases with increasing U value (Table I in the Supplemental Material [27]). Their

sum is shown in Fig. 13(a) and it eventually reaches the experimental value. On the other hand, the position of the main peak increases with increasing U and reaches maximum at 1.9 eV. Nonetheless, the position of this peak is way off the experimental value. The main peak position corresponds to the separation of the d-states. This implies that the calculations overestimate the energy distance between d-states by about 0.34 eV for $U_{\mathrm{eff}} = 0$ and 0.53 eV for $U_{\mathrm{eff}} = 1.9$ eV for Co.

The increase of the band energy distance with increasing U is also demonstrated in Fig. 13(b), showing linear increase of the optical and electronic band gap with U. The electronic band gap appears for $U \geqslant 1.14$ eV, as below this value the system is not a half metal, with part of the conduction band below the Fermi level.

Although tuning of U can well describe the saturation value of the magnetization, it does not correctly describe the main peak position due to overestimation of the energy distance between $3d$ bands. It demonstrates that a model of exchange-correlation potential other than GGA and GGA+U is needed
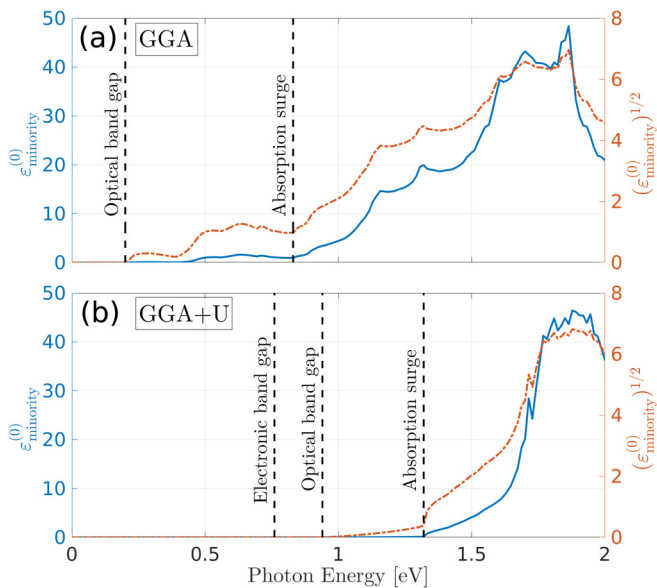

FIG. 12. Spectra of *ab initio* calculated unbroadened permittivity and its square root for minority spin electrons obtained by (a) GGA and (b) GGA+U potentials. The electronic band gap, optical band gap, and absorption surge are highlighted by vertical dashed lines.
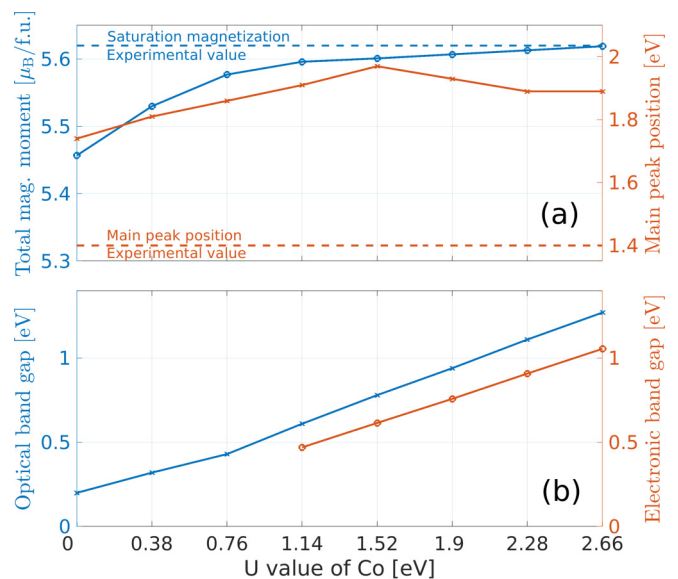

FIG. 13. Dependence of magnetic moments, band-gap energies, and main peak positions for various values of U_{eff} for Co. The ratio of the U values of Co and Fe is kept constant.

to better describe the electronic structure of CFAS (and 3*d* metals in general).

VII. DISCUSSION

The half metallicity of CFAS is claimed to be demonstrated by other experiments. In this section, we take a look at those experiments and discuss whether they contradict our observations.

The complicated nature of half metals makes direct observation of minority spin band gap difficult, thus indirect methods have to be employed and together with calculations provide enough evidence. The quantum nature of the phenomenon, together with the omnipresent spin-orbit coupling, present a difficult task.

Optical measurement of the electronic band gap was performed by Alhuwaymel *et al.* [23] using the reflection of circularly polarized infrared light. They determined the value of the band gap to be 0.11 eV at room temperature. However, their assumption of excitation of only minority spin electrons for left circularly polarized light seems incorrect, and thus this value is, in our opinion, not related to the band gap.

Several experiments have been conducted on magnetic tunnel junctions of $L2_1$ ordered CFAS/MgO/CFAS [22] and of CFAS/(MgAl$_2$)O$_x$/CoFe [11] exhibiting high TMR and high spin polarization of CFAS, suggesting its half-metallic character. However, their model does not include the spin-filtering effect of MgO [56], which may play a part in the high values of TMR. Nakatani *et al.* [30] measured the spin polarization of Co$_2$FeAl$_x$Si$_{1-x}$ by the point contact Andreev reflection in liquid helium, which resulted in maximum spin polarization of 0.60 for $x = 0.5$. These values are not high enough to conclude half metallicity. In our GGA calculations, only a single *d*-band crosses the Fermi level in the minority states. Furthermore, *d*-electrons are known for their localized nature and poor conductivity [57]. Despite the single *d*-band crossing the Fermi level, the Fermi level is approximately in the middle between the valence and conduction bands [Fig. 8(b)]. It may explain the observed temperature stability of CFAS, originally attributed to the Fermi level being in the middle of the band gap [11,12].

Fecher *et al.* [12] performed *ab initio* calculations of CFAS using the WIEN2K code [43] with the GGA+*U* potential resulting in the electronic band gap of 0.760 eV (with the Fermi level in the middle of the gap). As they have used the same code and parametrization, their results are identical to ours. Similar results were obtained by Gercsi *et al.* [25] using the OPENMX free software package with a band gap around 1 eV for GGA+*U* [$U_{\rm eff}$ = 2.1 (2.0) eV for Co (Fe)] and no band gap for GGA.

VIII. CONCLUSIONS

Spectral optical and magneto-optical properties of bulk Co$_2$FeAl$_{0.5}$Si$_{0.5}$ (CFAS) have been determined using ellipsometry and magneto-optical Kerr effect spectroscopy providing spectra of a full permittivity tensor. The spectra were theoretically described by the oscillator model and by *ab initio* calculations with various exchange-correlation potentials. We present an analysis that contradicts the general belief of half metallicity of CFAS, but seems not to contradict any of the already reported experiments. Namely, we show that CFAS probably has a pocket of minority *d*-electrons near point *X*.

The optical spectra reveal a dominant absorption peak at 1.40 eV originating from optical transitions of minority electrons, and its position corresponds to the separation of the occupied and excited minority *d*-states. The *ab initio* calculations systematically overestimate the position of this peak with the Hubbard *U* corrections shifting it even more. This indicates that the separation of the minority *d*-states is smaller than what the *ab initio* calculations predict. It also suggests that the Hubbard *U* correction does not improve the exchange-correlation potential to sufficiently describe the electronic structure of CFAS.

This leads to the conclusion that there probably are minority states at the Fermi level as a single *d*-band dips below it. Therefore, CFAS is likely not a HMF and could be classified as a type-III HMF [5] (which is technically not a half metal) with localized minority electrons at the Fermi level.

[1] R. A. de Groot, F. M. Mueller, P. G. van Engen, and K. H. J. Buschow, Phys. Rev. Lett. **50**, 2024 (1983).

[2] D. Tripathy, A. O. Adeyeye, and S. Shannigrahi, Phys. Rev. B **76**, 174429 (2007).

[3] J. Wang, P. Che, J. Feng, M. Lu, J. Liu, J. Meng, Y. Hong, and J. Tang, J. Appl. Phys. **97**, 073907 (2005).

[4] X.-H. Li, Y.-H. Huang, Z.-M. Wang, and C.-H. Yan, Appl. Phys. Lett. **81**, 307 (2002).

[5] C. Felser, G. H. Fecher, and B. Balke, Ang. Chem. Intl. Ed. **46**, 668 (2007).

[6] M. I. Katsnelson, V. Y. Irkhin, L. Chioncel, A. I. Lichtenstein, and R. A. de Groot, Rev. Mod. Phys. **80**, 315 (2008).

[7] T. Graf, C. Felser, and S. S. P. Parkin, Prog. Solid State Chem. **39**, 1 (2011).

[8] C. Felser, L. Wollmann, S. Chadov, G. H. Fecher, and S. S. P. Parkin, APL Mater. **3**, 041518 (2015).

[9] F. Ricci, S. Picozzi, A. Continenza, F. D'Orazio, F. Lucari, K. Westerholt, M. Kim, and A. J. Freeman, Phys. Rev. B **76**, 014425 (2007).

[10] S. Wurmehl, G. H. Fecher, V. Ksenofontov, F. Casper, U. Stumm, C. Felser, H.-J. Lin, and Y. Hwu, J. Appl. Phys. **99**, 08J103 (2006).

[11] R. Shan, H. Sukegawa, W. H. Wang, M. Kodzuka, T. Furubayashi, T. Ohkubo, S. Mitani, K. Inomata, and K. Hono, Phys. Rev. Lett. **102**, 246601 (2009).

[12] G. H. Fecher and C. Felser, J. Phys. D **40**, 1582 (2007).

[13] N. Tezuka, N. Ikeda, F. Mitsuhashi, and S. Sugimoto, Appl. Phys. Lett. **94**, 162504 (2009).

[14] S. S. P. Parkin, C. Kaiser, A. Panchula, P. M. Rice, B. Hughes, M. Samant, and S.-H. Yang, Nat. Mater. **3**, 862 (2004).

[15] A. Alfonsov, B. Peters, F. Y. Yang, B. Buchner, and S. Wurmehl, Phys. Rev. B **91**, 064421 (2015).

[16] M. Zhai, S. Ye, Z. Xia, F. Liu, C. Qi, X. Shi, and G. Wang, J. Supercond. Novel Magn. **27**, 1861 (2014).

[17] K. Wang, F. Ling, D. Gong, G. Wang, R. Chen, and Y. Huang, Mater. Chem. Phys. **214**, 355 (2018).

[18] A. Ruiz-Calaforra, A. Conca, T. Graf, F. Casper, B. Leven, C. Felser, and B. Hillebrands, J. Phys. D **46**, 475001 (2013).

[19] M. Yi, Z. F. Chen, D. X. Chen, S. Hiroaki, I. Koichiro, T. S. Lai, and S. M. Zhou, Chin. Phys. Lett. **28**, 067501 (2011).

[20] L. M. Loong, P. Deorani, X. P. Qiu, and H. Yang, Appl. Phys. Lett. **107**, 022405 (2015).

[21] Y. Wu, Y. L. Zhao, Q. Xiong, X. G. Xu, Y. Sun, S. Q. Zhang, and Y. Jiang, Chin. Phys. B **23**, 018503 (2014).

[22] H. Sukegawa, W. Wang, R. Shan, T. Nakatani, K. Inomata, and K. Hono, Phys. Rev. B **79**, 184418 (2009).

[23] T. F. Alhuwaymel, R. Carpenter, C. N. T. Yu, B. Kuerbanjiang, R. M. Abdullah, V. K. Lazarov, M. El-Gomati, and A. Hirohata, J. Appl. Phys. **117**, 17D131 (2015).

[24] B. Peters, Tuning the structural, magnetic and transport properties of full Heusler $Co_2FeAl_xSi_{1-x}$ compounds, Ph.D. thesis, The Ohio State University, 2014.

[25] Z. Gercsi and K. Hono, J. Phys.: Condens. Matter **19**, 326216 (2007).

[26] V. I. Anisimov, I. V. Solovyev, M. A. Korotin, M. T. Czyżyk, and G. A. Sawatzky, Phys. Rev. B **48**, 16929 (1993).

[27] See Supplemental Material at http://link.aps.org/supplemental/10.1103/PhysRevB.103.075146 for a detailed description of the oscillator functions, LDA results, and XRD Rietveld refinement.

[28] J. Rodríguez-Carvajal, Physica B **192**, 55 (1993).

[29] B. Balke, G. H. Fecher, and C. Felser, Appl. Phys. Lett. **90**, 242503 (2007).

[30] T. M. Nakatani, A. Rajanikanth, Z. Gercsi, Y. K. Takahashi, K. Inomata, and K. Hono, J. Appl. Phys. **102**, 033916 (2007).

[31] J. Hamrlová, D. Legut, M. Veis, J. Pištora, and J. Hamrle, J. Magn. Magn. Mater. **420**, 143 (2016).

[32] Š. Višňovský, Czech. J. Phys. B **36**, 1424 (1986).

[33] J. G. E. Jellison and J. S. Baba, J. Opt. Soc. Am. A **23**, 468 (2006).

[34] B. Johs and J. S. Hale, Phys. Status Solidi A **205**, 715 (2008).

[35] H. Fujiwara, *Spectroscopic Ellipsometry: Principles and Applications* (Wiley, Tokyo, 2007).

[36] *Complete EASE Data Analysis Manual* (J. A. Woollam Co., Inc., Lincoln, NE, 2011).

[37] T. E. Tiwald, D. W. Thompson, J. A. Woollam, W. Paulson, and R. Hance, Thin Solid Films **313–314**, 661 (1998).

[38] G. E. Jellison, Jr. and F. A. Modine, Appl. Phys. Lett. **69**, 371 (1996).

[39] G. E. Jellison, Jr. and F. A. Modine, Appl. Phys. Lett. **69**, 2137 (1996).

[40] D. De Sousa Meneses, M. Malki, and P. Echegut, J. Non-Cryst. Solids **352**, 769 (2006).

[41] K. E. Peiponen and E. M. Vartiainen, Phys. Rev. B **44**, 8301 (1991).

[42] T. D. Kang, H. S. Lee, and H. Lee, J. Korean Phys. Soc. **50**, 632 (2007).

[43] P. Blaha, K. Schwarz, G. K. H. Madsen, D. Kvasnicka, and J. Luitz, *WIEN2K, An Augmented Plane Wave + Local Orbitals Program for Calculating Crystal Properties* (Technische Universität Wien, Austria, 2001).

[44] T. Bandyopadhyay and D. D. Sarma, Phys. Rev. B **39**, 3517 (1989).

[45] R. Kubo, J. Phys. Soc. Jpn. **12**, 570 (1957).

[46] C. Ambrosch-Draxl and J. Sofo, Comput. Phys. Commun. **175**, 1 (2006).

[47] M. Cazzaniga, L. Caramella, N. Manini, and G. Onida, Phys. Rev. B **82**, 035104 (2010).

[48] A. Marini, G. Onida, and R. Del Sole, Phys. Rev. B **64**, 195125 (2001).

[49] J. A. Berger, P. Romaniello, R. van Leeuwen, and P. L. de Boeij, Phys. Rev. B **74**, 245117 (2006).

[50] A. J. Cohen, P. Mori-Sánchez, and W. Yang, Science **321**, 792 (2008).

[51] C. Cramer and D. Truhlar, Phys. Chem. Chem. Phys. **11**, 10757 (2009).

[52] S. A. Tolba, K. M. Gameel, B. A. Ali, H. A. Almossalami, and N. K. Allam, The DFT+U: Approaches, accuracy, and applications, in *Density Functional Calculations*, edited by G. Yang (IntechOpen, Rijeka, 2018), Chap. 1.

[53] J. Kübler, Physica B+C **127**, 257 (1984), Proceedings of the 4th General Conference of the Condensed Matter Division of the EPS.

[54] G. H. Fecher, H. C. Kandpal, S. Wurmehl, C. Felser, and G. Schönhense, J. Appl. Phys. **99**, 08J106 (2006).

[55] L. Makinistian, M. M. Faiz, R. P. Panguluri, B. Balke, S. Wurmehl, C. Felser, E. A. Albanesi, A. G. Petukhov, and B. Nadgorny, Phys. Rev. B **87**, 220402(R) (2013).

[56] C. Heiliger, P. Zahn, and I. Mertig, Mater. Today **9**, 46 (2006).

[57] J. Stöhr and H. Siegmann, *Magnetism: From Fundamentals to Nanoscale Dynamics*, Springer Series in Solid-State Sciences (Springer, Heidelberg, 2006).